Check for updates

Synthesis of Tostadas-Shaped Metal-Organic Frameworks for Remitting Capacity Fading of Li-Ion Batteries

Yueji Cai, Weikang Wang, Xuanxuan Cao, Lingfei Wei, Caichao Ye, Chunfeng Meng, Aihua Yuan,* Huan Pang,* and Chao Yu*

Electrode design strategies that aim to increase the electrochemical performance of Li-ion batteries (LIBs) play a key role in tapping into the power of the energy transformations involved. Metal-organic frameworks (MOFs) have attracted scientific interest as electrode materials for LIBs, while the utilization of pristine MOFs is hindered by limited conductivity and stability, partly due to their lack of hierarchically structured pores. Herein a hydrothermal-mechanical synthesis is reported by combining the one-pot chemical fabrication of $Ni_3(2,3,6,7,10,11-hexaiminotriphenylene)_2$ sheets and particles, and the mechanical assembly of these building blocks to improve electrical conductivity is also described. The as-prepared ensemble (denoted as NHM) exhibits a Tostadas-shaped structure with enriched ultramicropores and micropores. The charge-discharge profile of NHM gives a superior reversible capacity of 1280 mA h g^{-1} after 100 cycles at the rate of 0.1 A g^{-1}, surpassing the state-of-art pristine MOFs-based anodes. Moreover, NHM is capable of maintaining 392 mA h g^{-1} at 1 A g^{-1} after 1000 cycles, the completion of a stability test in coin cell-powered light emitting diodes further visualizes the remitted capacity fading of NHM. This work breaks through the limitation of capacity for pristine MOFs, providing a new pathway for achieving better energy conversion and storage.

1. Introduction

Currently, Li-ion batteries (LIBs) are the most popular energy storage source for high-tech applications such as portable electronic devices and power backup systems.[1] However, the cycle life and energy density of commercial LIBs still have not reached the specification demanded by customers. These

issues are mainly due to the low theoretical capacity of both commercial graphite anodes (372 mA h g^{-1}) and LiCoO$_2$ cathodes (172 mA h g^{-1}).[1a,2] Thus, it is necessary to make effort to develop alternatives of the LIBs electrode materials with longer cycle life, higher specific capacity, and better energy storage. Generally, carbon,[3] silicon,[4] and stannum[5] based materials are the most commonly used pristine materials in LIBs, while such pristine materials show limited capacity, rapidly decaying to lower performance after cycles.[3,6] Featured by the unique features of composition, pore structure, and functionality, the metal-organic frameworks (MOFs) were extensively investigated as pristine electrode materials for LIBs.[3,7] Controllable synthetic strategies of MOFs enable the optimization of metal ions/clusters, organic ligand linkers, the tunability of size, dimension, and morphology, leading to the improvement of the gravimetric/volumetric capacity, energy density, and long-term cyclability of LIBs. Although there are more than 20 000 kinds of MOFs synthesized so far, pristine MOFs, when utilized as electrode materials in LIBs, also suffer from inevitable fading in rate capability and electrical conductivity.[8] For example, the typical transition metal MOFs such as Zn$_4$O-BTC MOF delivered a capacity of 105 mA h g^{-1} in 50 cycles and Ni-NTC MOF showed a capacity of 246 mA h g^{-1} in 80 cycles (Table S1, Supporting Information). The maximum capacity of pristine MOFs in the 100 cycles can be achieved at 1085 mA h g^{-1} by regulating the morphology of Ni-BTC MOFs, which highlights the importance of controlling dimension and structure in optimizing the rate capacity of pristine MOFs materials.[9]

Herein, a mechanical ball-milling assisted hydrothermal method was exploited to obtain the pristine Ni-MOF based electrodes with superior and long-operating LIBs performance. First, the Ni$_3$(2,3,6,7,10,11-hexaiminotriphenylene)$_2$ (Ni-HITP) nanosheets (NHS) and Ni-HITP particles (NHP) materials were both fabricated through a one-pot solvothermal method.[10] The structures of NHS and NHP are similar to the Ni-BTC and have excellent conductivity. Granular NHP has a high initial specific capacity, but the specific capacity is prone to decay. On the contrary, the initial specific capacity of NHS is low while the cyclic stability is prominent. To integrate both advantages, the further assembly of nanosheets and nanoparticles was simply

Y. J. Cai, W. K. Wang, X. X. Cao, L. F. Wei, C. F. Meng, A. H. Yuan, C. Yu
School of Environmental and Chemical Engineering
Jiangsu University of Science and technology
Zhenjiang, Jiangsu 212100, P. R. China
E-mail: aihuayuan@163.com; chao_yu@just.edu.cn
C. C. Ye
Academy for Advanced Interdisciplinary Studies & Guangdong
Provincial Key Laboratory of Computational Science and Material Design
Southern University of Science and Technology
Shenzhen, Guangdong 518055, P. R. China
H. Pang
School of Chemistry and Chemical Engineering
Yangzhou University
Yangzhou, Jiangsu 225009, P. R. China
E-mail: panghuan@yzu.edu.cn

The ORCID identification number(s) for the author(s) of this article can be found under https://doi.org/10.1002/adfm.202109927.
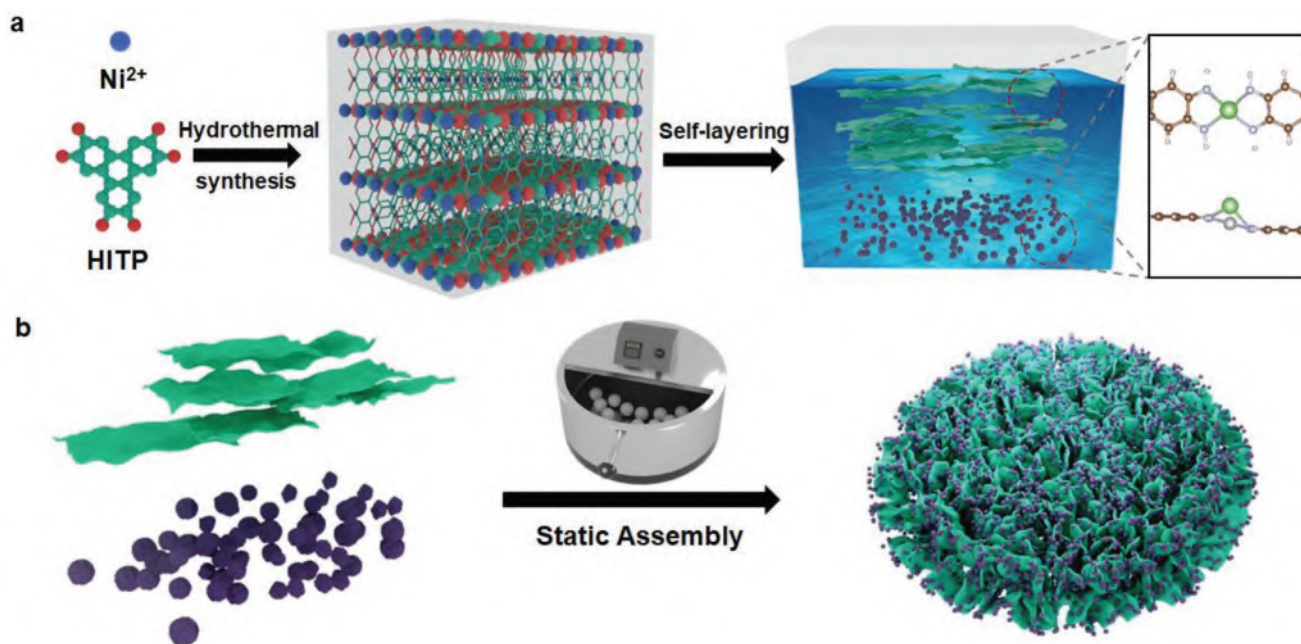
achieved by the mechanical electrostatic assembly among the ball-milling treatment, resulting in a hierarchical Ni-MOF nanostructure (the ensemble of NHS and NHP, denoted as NHM), with optimized pore and channels. Compared to previous reported pristine MOFs anodes, NHM, benefiting from the multiscale integration of 2D nanosheets and 1D nanoparticles, affords an ultrahigh capacity (1280 mA h g^{-1} at 0.1 A g^{-1} after 100 charge-discharge cycles) and remitted capacity fading (392 mA h g^{-1} at a high rate of 1 A g^{-1}, after 1000 cycles), which is comparable with most of the composite materials applied in LIBs anode (Table S1, Supporting Information).

2. Results and Discussion

Scheme 1 illustrates the hydrothermal-mechanical synthesis process of NHM architecture. In a typical synthesis process, 2,3,6,7,10,11-hexaaminotriphenylene hexahydrochloric acid (HITP·6HCl) solution was transferred to NiCl$_2$/NH$_4$OH solution and the reaction mixture was heated under constant stirring at 65 °C for 2 h, and then without stirring for 13 h. Due to the gravity and surface tension, two morphologies of obtained Ni-HITP MOF were self-layering with Ni-HITP nanosheets (NHS) up in the liquid phase as well as Ni-HITP particles (NHP) settling down at the bottom. Mechanical ball-milling was introduced and mechanical ball-milling induced assembly of NHS and NHP was attempted in different conditions, using an SFM-1 mixer mill (50-mL agate milling jar with 5, 8, and 12-mm diameter agate ball). As shown in Figure S1, Supporting Information, electrostatic assembly of building blocks, namely NHS and NHP, is driven by the mechanical force through precise regulation of milling parameters under N$_2$ protection. An organized structure that resembles the Tostadas shape, arises from opposing interactions between controlled moving components that exist out of initial equilibrium and subsequently reduce its free energy and move towards a new state. The unique integration of NHS and NHP into NHM can provide the channels that generate the special framework and which can contribute to facile ion transport. The conductivity of each NHM structural model was determined through the partial density of states (PDOS) calculation. The structural characteristics prove that the Ni metal coordination of N contributes to improving the adsorption capacity for Li (Figure S2, Supporting Information). The transmission electron microscope (TEM) images in Figure S3 and Figure S4, Supporting Information, show the morphology of NHM. As shown in Figure S3a, Supporting Information, the interconnected nanosheets of Ni-HITP were closely wrapped with the nanoparticles with a size of ≈10 nm. Moreover, the lattice fringes of NHM can be well detected (Figure S3b, Supporting Information), and the diffraction rings along the distinct bright spots confirm the polycrystalline nature in the prepared Ni-HITP-based MOFs (Figure S3c, Supporting Information). According to the selected area electron diffraction (SAED) pattern in Figure S3d, Supporting Information, the measured d-spacing of 10 Å and d-spacing of 2 Å corresponds to the crystalline (200) and (100) plane of Ni-HITP in NHM, respectively.[11] Consequently, the crystalline nature of Ni-HITP can be easily recognized from the high-resolution TEM image of the NHM and SAED pattern.

The as-synthesized NHP, NHM, and NHS were further analyzed by X-ray Diffraction (XRD) in the 2θ range of 4°–40°. In **Figure 1**a, the dominant peaks observed at 4.7°, 9.5°, 12.6°, and 16.5° indicates the long-range crystallinity order along the *ab* plane.[12] All the three samples reveal-well defined (100) and (200) planar peaks at 4.7° and 9.5°. Meanwhile, a broad peak at 27.3° matching the (001) crystal plane of NHM indicates the poorer long-range order along the *c*-axis, which is commonly observed in covalently bonded layered materials.[13] The

Scheme 1. a) Schematic illustration of the one-pot solvothermal formation of 1D NHP and 2D NMS. b) Mechanical electrostatic assembly of NHP and NHS into Tostadas-shaped NHM by controlled ball-milling treatment.
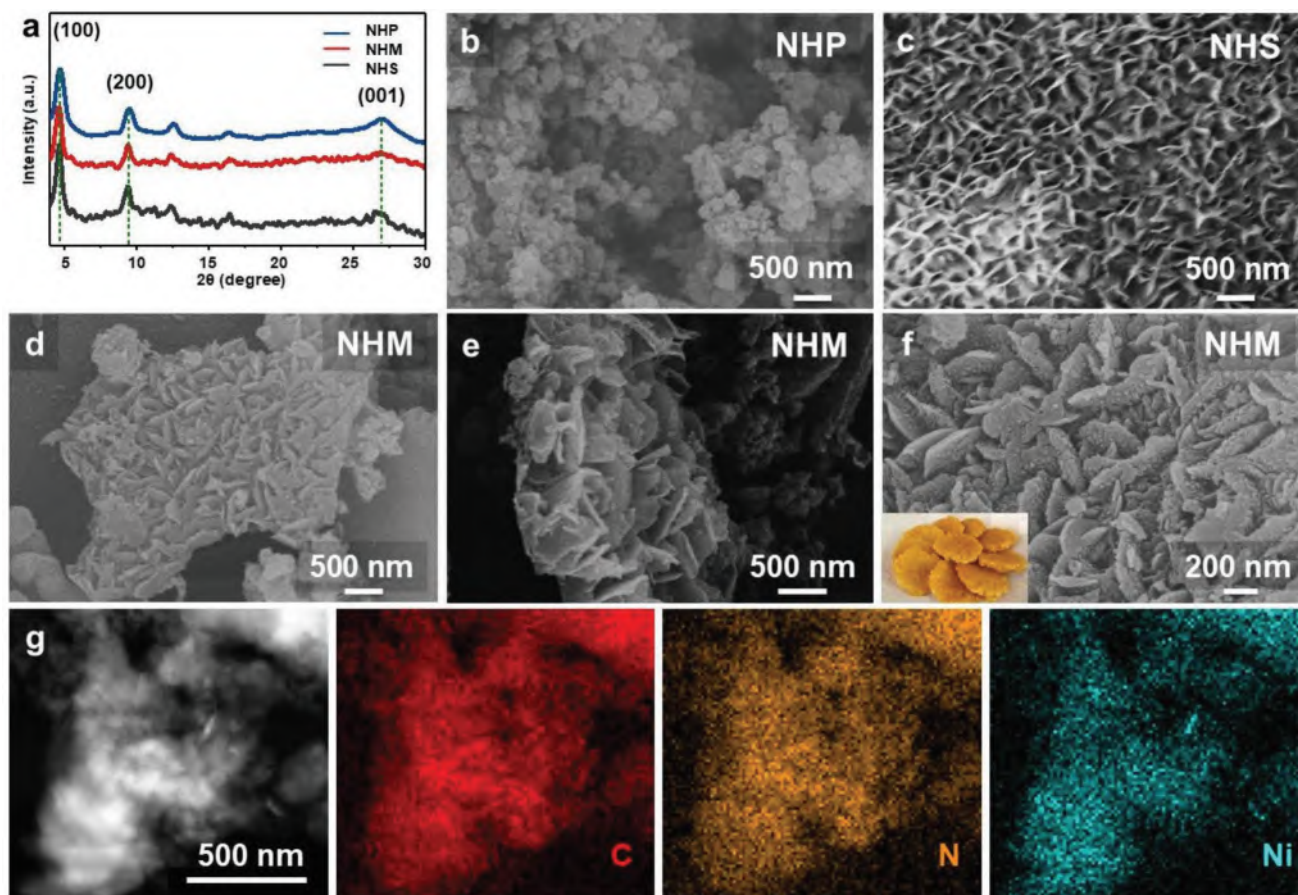
Figure 1. a) XRD patterns of the Ni-HITP; b) SEM images of NHP; c) SEM images of NHP; d–f) SEM images of Tostadas-shaped NHM in the scales of 500 and 200 nm; g) Energy Dispersive Spectrometer elemental mapping of the NHM.

morphologies of the NHS, NHP, and NHM samples were studied by the scanning electron microscope (SEM). Figure 1b and Figure S5, Supporting Information, show that the NHP sample displays a particle size with an average diameter of around 50 nm, while for NHS, the nanosheets-like Ni-HITP is constructed in an interwoven pattern (Figure 1c). After the pore engineering of ball-milling treatment, the size of NHP decreases obviously,[14] smaller than 10 nm, and meanwhile a unique Tostadas-shaped pristine NHM is achieved with 1D NHP embedded onto 2D nanosheets of NHS (Figure 1d–f, Figure S6, Supporting Information). The elemental mapping of TEM was then employed to confirm the elemental distribution of the Ni-HITP in the NHM. As depicted in Figure 1g, the characteristic elements for NHM including C, N, and Ni are evenly distributed on the surface of the NHM, indicating the controllable fine-tuning of mechanical electrostatic assembly. After moving, positioning, interconnecting, and contacting nanostructures during the ball-milling, the obtained framework makes Li$^+$ rapidly accessible to targeted redox-active sites, as well as ensures a high-efficiency electron transfer around the active center.[12a,15]

The Fourier-transform infrared (FTIR) spectra were used to identify the functional groups of each sample. Figure S7, Supporting Information, shows several peaks at 3345, 3180, 1620, and 1300 cm^{-1}, corresponding to the stretching vibrations of

N—H and C—N and the in-plane bending vibrations of N—H, respectively. The existence of rich N-containing groups of NHM is favorable for improving the conductivity of MOFs materials.[17] Furthermore, the thermogravimetric analysis (TGA) for NHM reveals an apparent weight loss began at 275 °C for all samples and also demonstrates that NHM possesses higher thermal stability than NHP (Figure S8, Supporting Information). In Figure S9, Supporting Information, Raman spectra of NHP, NHS and NHM shows that $i(D)/i(G)_{NHM} > i(D)/i(G)_{NHS} = i(D)/i(G)_{NHP}$ corresponding to more defects and active sites in NHM. The chemical states of surface elements in Ni-HITP based materials were characterized by X-ray photoelectron spectroscopy (XPS). As shown in **Figure 2**a,b and Figure S10, Supporting Information, Ni 2p peaks for NHM can be fitted with four prominent peaks at binding energies of 854.36, 860.30, 871.94, and 878.30 eV, corresponding to Ni 2p$_{3/2}$, Ni 2p$_{3/2}$ satellite, Ni 2p$_{1/2}$, and Ni 2p$_{1/2}$ satellite (Figure 2a).[16] Accordingly, the spectra of N 1s for NHM display two prominent peaks at 399.0 eV and 400.2 eV, belonging to N—C, N—Ni, respectively (Figure 2b), in good agreement with the FTIR results. The N 1s peaks for NHM can be resolved into two components centered at ≈398.98 (N—C), and ≈400.18 eV (N—Ni). Specifically, Ni metal centers attached with HITP^{-2} ligands in the woven net pattern form a highly porous morphology, increasing the surface area of the MOF.[17] Thereby, the content of active sites
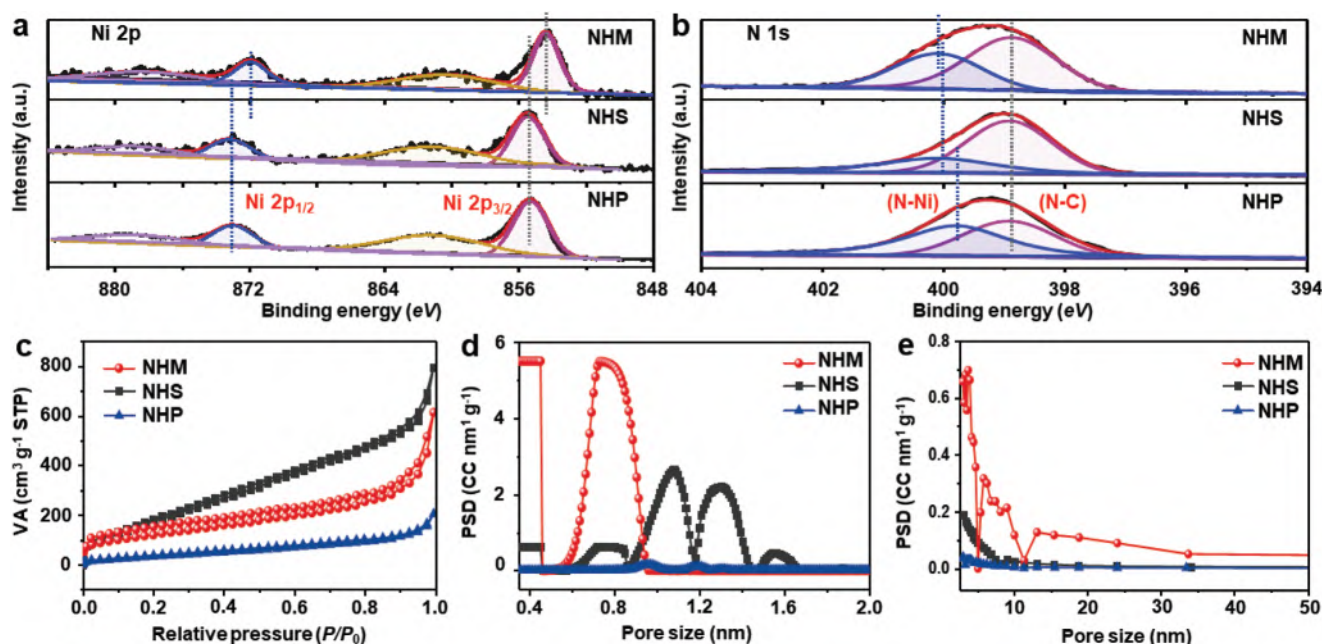
Figure 2. a,b) High-resolution XPS spectra of Ni 2p and N 1s on NHM, NHS, and NHP; c) N_2 adsorption-desorption isotherm of NHM, NHS, and NHP at 77.3 K; d) Barrett–Joyner–Halenda (BJH) pore size distribution of NHM, NHS, and NHP; e) Saito-Foley method pore size distribution of NHM, NHS, and NHP.

can be defined as the ratio of peak areas (N−Ni/N−C).[18] The XPS results manifest the existence of active sites in NHP, NHS, and NHM, and the corresponding active site contents are 1.03, 1.09, and 1.11 in the order of NHP < NHS < NHM. Compared with the NHP and NHS, the Ni 2p peaks of NHM obviously shift toward low binding energy (Figure 2a) after electrostatic assembly by ball-milling process. The lower binding energy of exposed active Ni sites indicates the gained electrons from adjacent N atoms, leading to the decreased valence state of Ni of NHM. The nearly metallic state of Ni species generated in the construction process of NHM is conducive to charge transfer and tuned redox potential.[19]

The surface area and pore distribution of NHM, NHS, and NHP were studied by N_2 adsorption-desorption isotherms as shown in Figure 2c. The Brunauer–Emmett–Teller (BET) specific surface area of NHM was determined to be 445 m^2 g^{-1}, mainly ascribed to the enriched ultramicropores and micropores provided by pore engineering through ball-milling, as can be seen in pore size analysis within different ranges (Figure 2d,e).[20] Obviously, the NHM exhibits a wide pore distribution ranging less than 0.6 nm (defined as ultramicropore),[21] which could support the storage behavior of pseudo-capacitive lithium.[18] Moreover, these ultramicropores and micropores of hierarchical NHM could selectively block the large anions owing to the size effect, leading to the better redistributing of Li-ion flux.[22] This homogeneous plating/stripping process would result in an ultrahigh capacity with remitted capacity fading for NHM anode.

Based on the aforementioned characteristics of porous structures and chemical properties, the electrochemical performance of obtained NHP, NHS, and NHM anodes was then investigated through LAND device. The capacity of NHM with 10% NHS was superior to that of the other Ni-HITP electrodes

in control experiment (more details of Ni-HITP with different contents of NHS can be seen in Figure S11, Supporting Information). **Figure 3**a shows the cyclabilities of NHP, NHS, and NHM. In the first cycle, the discharge capacities for NHP, NHS, and NHM are 397, 1787, and 946 mA h g^{-1}, respectively. After 100 cycles, their capacities reduced to 105, 1280, and 497 mA h g^{-1}, respectively. The achieved maximum reversible capacity of 1280 mA h g^{-1} was found for the NHM electrode after 100 cycles, suggesting an outstanding LIBs activity. Ni-based MOF LIBs anodes that can maintain 1000 mA h g^{-1} after 100 cycles are rarely reported (Table S1, Supporting Information).[8a] This remarkable performance could be attributed to the ensemble effect within the Tostadas-shaped structure and the decreased valence state of Ni active center.

The rate capabilities of the NHS, NHM, and NHP were also evaluated by increasing the rate from 0.1 to 2 A g^{-1} (Figure 3b). The capacity of NHM is 950 mA h g^{-1} at 0.1 A g^{-1}. As the current density increases, reversible capacities of NHM reach 754, 572, and 366 mA h g^{-1} at 0.2, 0.5, and 2 A g^{-1} for the NHM electrode. The NHM electrode retrieves a capacity of 800 mA h g^{-1} when the current density restores to 0.1 A g^{-1}. This is a value close to its original value of 950 mA h g^{-1}, showing the excellent electrochemical stability of NHM. For the NHS and NHP electrodes, their reversible capacities of 716 and 537 mA h g^{-1} are delivered at 0.1 A g^{-1}, which decrease rapidly to 129 and 84 mA h g^{-1} at 2000 mA g^{-1}, respectively. The corresponding charge-discharge profiles of these three electrodes at various rates are shown in Figure 3c. The charge-discharge profiles of the NHM electrode stay on hold without evident variance even at high rates. The charge-discharge profiles of NHS and NHP, by contrast, appear severe variances at 2000 mA g^{-1}. These results suggest that the rate performance of NHM is considerably improved by tuning its morphology.[23]
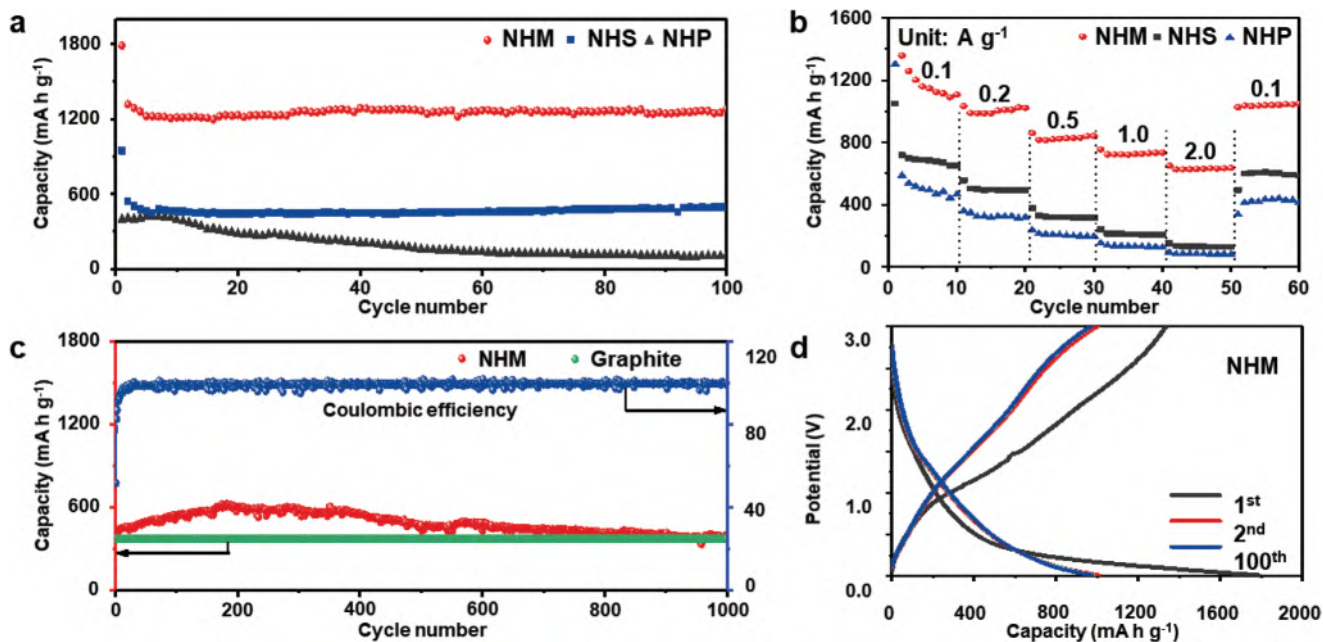
Figure 3. a) Cycling performance of NHP, NHM, and NHS over 100 cycles at 0.1 A g^{-1}; b) Rate capabilities of NHS, NHM, and NHP at the rate from 0.1 to 2 A g^{-1}; c) Cyclability and corresponding coulombic efficiency of the NHM at the rate of 1 A g^{-1}; d) NHM galvanostatic charge-discharge potential profiles at the rate of 0.1 A g^{-1}.

We further performed a long-term cyclability at a high rate of 1000 mA g^{-1} to test the rapid charging and discharging capacity of NHM anode (Figure 3c). Specially, the capacity of the NHM electrode increases from 414 to 576 mA h g^{-1} in the initial 200 cycles, and remains stable at this value until 380 cycles. Subsequently, it descended slowly, reaching 392 mA g^{-1} at 1000 cycles, which is still better than theoretical value of commercial graphite anodes (372 mA h g^{-1}). Figure 3d and Figure S12, Supporting Information, shows the typical charge/discharge curves of the NHS, NHM, and NHP electrode at a current density of 0.1 A g^{-1}. In all the view of Figure 3d and Figure S12, Supporting Information, the initial charge/discharge curves of first cycle show the growing formation of solid-electrolyte interphase (SEI) layer on the surface of electrodes.[24] In the following cycles, the charge/discharge curves of NHM overlap much better than NHS and NHP, suggesting good stability and significant reversibility of the NHM electrode for the insertion/extraction of Li$^+$, corresponding to Figure S13, Supporting Information.[25] Meaningfully, the sloping voltage profiles suggest the pseudocapacitive lithium storage behavior, which could reduce the polarization of LIB and improve the stability of the electrodes.[22,26] These results with remitted capacity fading are attributed to the Tostadas-shaped architecture of NHM built by the strong electrostatic adsorption of NHP on the NHS, which shortens the diffusion distance of Li ions, thus maintaining the sustainability in the repeated activation process of the NHM electrode.

To further investigate the electrochemical performance and interface resistance of NHM electrodes, more electrochemical measurements were performed. **Figure 4**a displays the cyclic voltammetry (CV) of the NHM electrodes for an initial three cycles, revealing two reduction peaks and two oxidation peaks. For the first cathodic sweep, the current slowly increases in the potential range from the open circuit potential (OCP) to about 1.4 V versus Li/Li$^+$. This phenomenon corresponds to the decomposition of the electrolyte (LiPF$_6$ in ethylene carbonate/dimethyl carbonate) on the electrode surface to form an SEI layer.[24,27] Furthermore, from 0.95 to 0.7 V versus Li/Li$^+$, the cathodic current of NHM continues to increase. This can be ascribed to the lithiation of carbonaceous material (Super P carbon black, Ni-HITP) to generate Li$_x$C or Li$_x$O on the surface of the electrode. Meanwhile, as Figure 4a shown, two tiny peaks at 0.42 and ≈1.4 V can be observed in the second and third cathodic scans. They can be assigned to the reduction reaction of Ni^{2+} to Ni^0. During anodic scanning, NHM shows two oxidation peaks at 1.01 and 2.17 V versus Li/Li$^+$. The two peaks can be ascribed to the conversion of Ni^0 to Ni^{1+} and Ni^{1+} to Ni^{2+}, respectively.[28] From the second scanning onward, the cathodic curves of NHM appear to be distinct from the first cycle curve. This is also attributed to the formation of the SEI film on the electrode surface. This result demonstrates that the presence of NHM facilitates the alloying and dealloying with Li.[23b]

To clarify the high specific capacity and electrochemical stability of the NHM and the formation mechanism of SEI layer, electrochemical impedance measurements were performed on the NHS, NHP, and NHM electrodes, as shown in Figure 4b. It is noticeable that the NHM electrode has a smaller charge transfer resistance (R_{ct}) than the NHP electrode. Meanwhile, R_{ct} of NHS is slightly less than NHM. NHS has the minimum impedance among three samples as monolayers of nanosheets materials are known for their widely dispersed valence and conduction bands, facilitating the charge mobility within 2D sheets.[29] To prove the formation of the SEI layer and its growth in subsequent cycles, the electrochemical impedance spectra of the NHM electrode after 1, 3, 100, and 200 cycles were recorded in Figure 4c. The magnitude of the semicircles
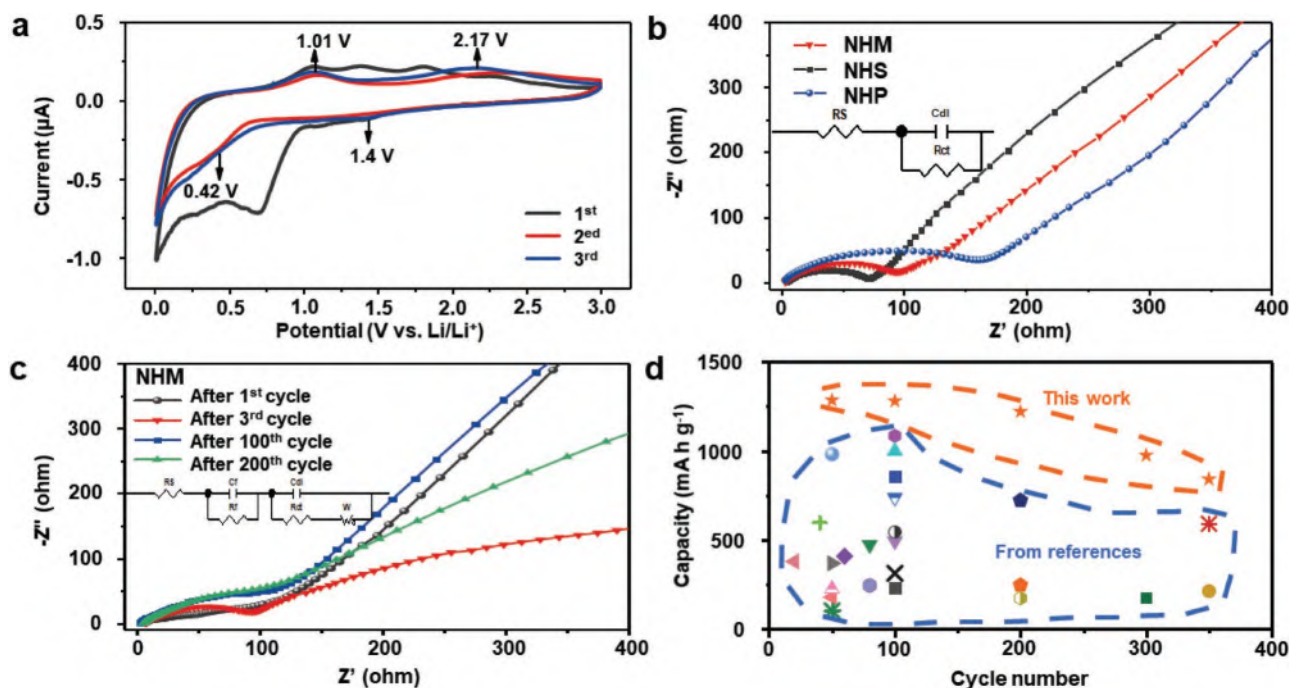
Figure 4. a) CVs of NHM electrodes, recorded at the scan rate of 0.1 mV s^{-1}; b) Impedance spectra of NHS, NHM, and NHP electrodes; c) Impedance spectra of the NHM electrodes after several cycles of charge-discharge; d) The capacity comparison between NHM electrodes and other MOFs-based electrodes in related publications (see details in Table S1, Supporting Information).

remains almost unchanged for the first three cycles of charge-discharge, suggesting a stable SEI layer. Also, the 100th and 200th cycles of charge-discharge imply that SEI layer could be in good condition. Figure 4d demonstrates an ultrahigh capacity (1280 mA h g^{-1} at 0.1 A g^{-1} after 100 charge-discharge cycles) and robust cycling stability of as-synthesized NHM, which is surpass the most of reported MOF-based LIBs anode materials (Table S1, Supporting Information). In this work, Hydrothermal-Mechanical synthesis reduces the size of NHP in NHM together with reducing the thickness of NHS to increase the proportion of ultramicropores and micropores that are critical to providing efficient channels for the Li$^+$ ions percolation towards the electrode.[30]

To investigate the pseudocapacitive lithium storage behavior of NHP, NHS, and NHM electrodes, the CV measurements at different sweep rates from 0.2 to 1.2 mV s^{-1} were carried out. As shown in **Figure 5**a and Figure S14a,b, Supporting Information, the CV curves of all three samples exhibit a uniform shape. Among the NHP, NHS, and NHM, there is no significant redox peak in NHS, while CV curves of NHP exhibit two dominating pairs of redox peaks, and a pair of further apart redox peaks illustrates in CV curves of NHM.[31] Figure 5b presents the capacitive contribution areal which occupies about 55% of the total capacity for NHM at 0.6 mV s^{-1}.[9a] The peak current in the CV curves obeys a power-law relationship with the sweep rate according to the formula: $i = a v^b$.[32] In general, the b-value of 0.5 indicates a diffusion-controlled process, whereas 1.0 suggests a capacitive process.[33] Consequently, Figure 5c depicts the $\log(i)$-$\log(v)$ plots for the NHP, NHS, and NHM electrode. At the low sweep rates from 0.2 to 1.2 mV s^{-1}, the b-value is 0.59 for the anodic peaks and 0.57 for the cathodic peaks in

NHM, suggesting that the capacitive process is dominant. The b-value decreases to 0.48 for the anodic peaks and 0.47 for the cathodic peaks in NHS at the low sweep rates from 0.2 to 1.2 mV s^{-1}, suggesting that the diffusion process is dominant. Similarly, the b-value decreases to 0.39 for the anodic peaks and 0.38 for the cathodic peaks in NHP at the low sweep rates from 0.2 to 1.2 mV s^{-1}, suggesting that the diffusion process is dominant.[34] As shown in Figure 5d, the capacitive domination of the total capacity in NHM are 47, 52, 55, 76, 82, and 88% at 0.2, 0.4, 0.6, 0.8, 1.0, and 1.2 mV s^{-1}, which are much better than NHS and NHP. It can be concluded that the electrochemical kinetic control of NHS and NHP is diffusion control, while the kinetic control of NHM obtained by hydrothermal-mechanical synthesis transforms into pseudocapacitance control. This also explains the high specific capacity and stability of the NHM electrode.[35] Furthermore, actual tests on the battery were carried out by assembling coin cells. The change rule of light emitting diode (LED) brightness powered by prepared MOFs-based anodes is consistent with their electrochemical results (Figure 5e,f). Compared to NHS and NHP, NHM displays an ultrahigh capacity and imperceptible capacity fading visualized in the LED lights.

3. Conclusion

In summary, we highlight a hydrothermal-mechanical synthetic design to boost lithium storage properties of pristine MOF anodes by a facile interface engineering. A Tostadas-shaped architecture (NHM) was constructed with Ni-HITP nanosheets (NHS) and Ni-HITP nanoparticles (NHP) as building blocks
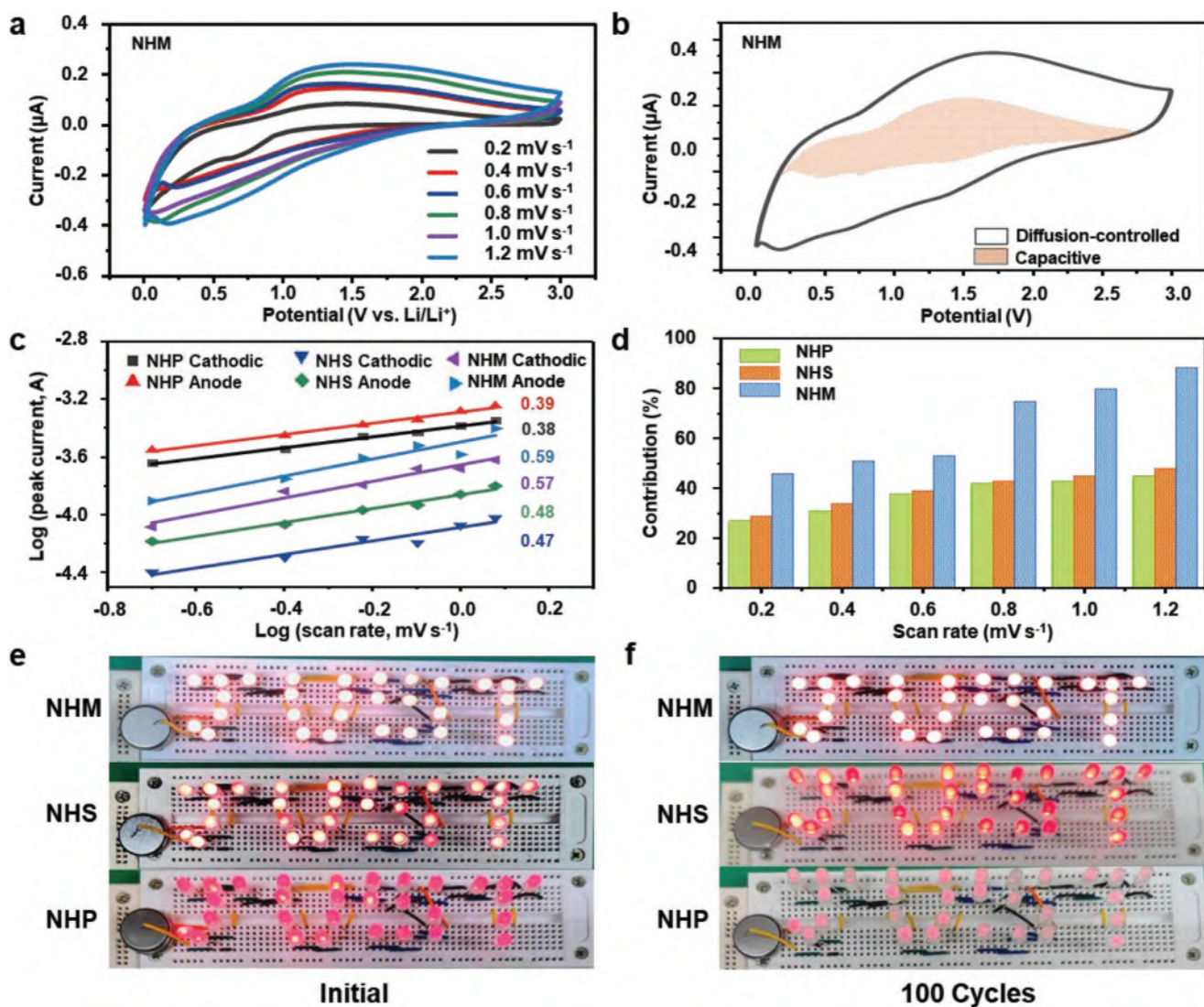
Figure 5. a) CV curves at different scan rates from 0.2 to 1.2 mV s^{-1} of NHM; b) Separation of the capacitive and diffusion-controlled currents of NHM at the scan rate of 1 mV s^{-1}; c) The relationship between log(i) against log(ν) for NHS, NHP, and NHM; d) Relative contributions of the capacitive and diffusion-controlled behavior at different scan rates; e) Illuminated LED lights powered by NHM, NHS, and NHP in their initial state; f) Illuminated LED lights powered by NHM, NHS, and NHP after 100 cycles.

through the combination of one-pot chemical synthesis and mechanical electrostatic assembly. Furthermore, the relationship between the special morphology and pseudocapacitive behavior of as-prepared NHM anode was evaluated. The optimal reversible capacity of NHM remained 1280 mA h g^{-1} after 100 cycles of charge-discharge at the rate of 0.1 A g^{-1}, which is superior to those of reported pristine MOFs under the same conditions. The kinetic pseudocapacitance control of NHM was proved to be a key factor in improving lithium storage capacity and stability, which is related to the unique pore structure and element state endowed by the formation process of Tostadas shape. Actual test that assembled NHM in coin cells further showcases its superior resistance to the capacity fading as conventional pristine MOFs fail. This work provides an ideal alternative anode candidate to optimize the capacities, rate, and cycling performances for lithium-ion batteries, further paving a new pathway for composite material aiming at record-breaking performance.

Supporting Information

Supporting Information is available from the Wiley Online Library or from the author.

Acknowledgements

Conflict of Interest

The authors declare no conflict of interest.

Data Availability Statement

Research data are not shared.

Keywords

[1] a) J. T. Deng, L. Wang, J. Deng, Y. Fang, Y. Lin, Y. H. Hu, *J. Mater. Chem. A* **2020**, *8*, 3397; b) T. Zhou, J. Shen, Z. Wang, J. Liu, R. Hu, L. Ouyang, Y. Feng, H. Liu, Y. Yu, M. Zhu, *Adv. Funct. Mater.* **2020**, *30*, 1909159; c) X. Chen, G. Xu, X. Ren, Z. Li, X. Qi, K. Huang, H. Zhang, Z. Huang, J. Zhonga, *J. Mater. Chem. A* **2017**, *5*, 6581.

[2] a) D. Cai, M. Lu, L. Li, J. Cao, D. Chen, H. Tu, J. Li, W. Han, *Small* **2019**, *15*, 1902605; b) C. F. Meng, P. F. Hu, H. T. Chen, Y. J. Cai, H. Zhou, Z. H. Jiang, X. Zhu, Z. Y. Liu, C. Y. Wang, A. H. Yuan, *Nanoscale* **2021**, *13*, 7751; c) X. Zhao, V.-P. Lehto, *Nanotechnology* **2021**, *32*, 042002; d) D. Ma, Y. Li, J. Yang, H. Mi, S. Luo, L. Deng, C. Yan, M. Rauf, P. Zhang, X. Sun, X. Ren, J. Li, H. Zhang, *Angew. Chem., Int. Ed.* **2018**, *28*, 1705537.

[3] Z. Zhao, S. Das, G. Xing, P. Fayon, P. Heasman, M. Jay, S. Bailey, C. Lambert, H. Yamada, T. Wakihara, A. Trewin, T. Ben, S. Qiu, V. Valtchev, *Angew. Chem., Int. Ed.* **2018**, *57*, 11952.

[4] a) Y. Yang, S. Wu, Y. Zhang, C. Liu, X. Wei, D. Luo, Z. Lin, *Chem. Eng. J.* **2021**, *406*, 126807; b) H. Tian, H. Tian, W. Yang, F. Zhang, W. Yang, Q. Zhang, Y. Wang, J. Liu, S. P. Silva, H. Liu, G. Wang, *Adv. Funct. Mater.* **2021**, *31*, 2101796.

[5] a) I. S. Aminu, H. Geaney, S. Imtiaz, T. E. Adegoke, N. Kapuria, G. A. Collins, K. M. Ryan, *Adv. Funct. Mater.* **2020**, *30*, 2003278; b) D. Ma, Y. Li, H. Mi, S. Luo, P. Zhang, Z. Lin, J. Li, H. Zhang, *Angew. Chem., Int. Ed.* **2018**, *57*, 8901.

[6] a) M. Ge, C. Cao, G. M. Biesold, C. D. Sewell, S.-M. Hao, J. Huang, W. Zhang, Y. Lai, Z. Lin, *Adv. Mater.* **2021**, *33*, 2004577; b) L. Wu, J. Zheng, L. Wang, X. Xiong, Y. Shao, G. Wang, J.-H. Wang, S. Zhong, M. Wu, *Angew. Chem., Int. Ed.* **2019**, *58*, 811; c) X. Zhou, Q. Liu, C. Jiang, B. Ji, X. Ji, Y. Tang, H.-M. Cheng, *Angew. Chem., Int. Ed.* **2020**, *59*, 3802; d) X. Gao, Y. Dong, S. W. Li, J. W. Zhou, L. Wang, B. Wang, *Electrochem. Energy Rev.* **2020**, *3*, 81.

[7] a) S. Chae, S.-H. Choi, N. Kim, J. Sung, J. Cho, *Angew. Chem., Int. Ed.* **2020**, *59*, 110; b) X. Y. Shi, Y. Y. Shan, M. Du, H. Pang, *Coord. Chem. Rev.* **2021**, *444*, 214060.

[8] a) J. Zhang, J. Wan, J. Wang, H. Ren, R. Yu, L. Gu, Y. Liu, S. Feng, D. Wang, *Angew. Chem., Int. Ed.* **2019**, *58*, 5266; b) P. Wang, H. Zhou, C. F. Meng, Z. T. Wang, K. Akhtar, A. H. Yuan, *Chem. Eng. J.* **2019**, *369*, 57; c) X. C. Han, P. Liu, F. Lin, W. Q. Chen, R. C. Luo, Q. Han, Z. Jiang, X. D. Wang, S. X. Song, K. M. Reddy, H. X. Deng, M. W. Chen, *Angew. Chem., Int. Ed.* **2020**, *59*, 21419; d) H. Tian, H. Tian, S. Wang, S. Chen, F. Zhang, L. Song, H. Liu, J. Liu, G. Wang, *Nat. Commun.* **2020**, *11*, 5025.

[9] a) S. H. Lim, G. D. Park, Y. C. Kang, *Chem. Eng. J.* **2020**, *401*, 126121; b) H.-H. Fan, L. Zhou, H.-H. Li, C.-Y. Fan, X.-L. Wu, J.-P. Zhang, *2D Mater.* **2019**, *6*, 045022; c) J. Yang, F. J. Zhang, H. Y. Lu, X. Hong,

[9] H. L. Jiang, Y. Wu, Y. D. Li, *Angew. Chem., Int. Ed.* **2015**, *54*, 10889; d) X. Guo, C. Chen, Y. Zhang, Y. Xu, H. Pang, *Energy Storage Mater.* **2019**, *23*, 439.

[10] a) E. M. Miner, T. Fukushima, D. Sheberla, L. Sun, Y. Surendranath, M. Dinca, *Nat. Commun.* **2016**, *7*, 10942; b) Y. S. Wei, L. L. Zou, H. F. Wang, Y. Wang, Q. Xu, *Adv. Energy Mater.* **2021**, *11*, 2003970.

[11] D. Sheberla, L. Sun, M. A. Blood-Forsythe, S. Er, C. R. Wade, C. K. Brozek, A. Aspuru-Guzik, M. Dinca, *J. Am. Chem. Soc.* **2014**, *136*, 8859.

[12] a) D. Sheberla, J. C. Bachman, J. S. Elias, C.-J. Sun, Y. Shao-Horn, M. Dinca, *Nat. Mater.* **2017**, *16*, 220; b) M. E. Foster, K. Sohlberg, M. D. Allendorf, A. A. Talin, *J. Phys. Chem. Lett.* **2018**, *9*, 481.

[13] F. B. Ajdari, E. Kowsari, M. N. Shahrak, A. Ehsani, Z. Kiaei, H. Torkzaban, M. Ershadi, S. K. Eshkalak, V. Haddadi-Asl, A. Chinnappan, S. Ramakrishna, *Coord. Chem. Rev.* **2020**, *422*, 213441.

[14] T. Zeng, G. He, X. Li, C. Wang, *J. Appl. Polym. Sci.* **2021**, *138*, 50790.

[15] Z. A. Ghazi, X. He, A. M. Khattak, N. A. Khan, B. Liang, A. Iqbal, J. X. Wang, H. S. Sin, L. S. Li, Z. Y. Tang, *Adv. Mater.* **2017**, *29*, 1606817.

[16] M. G. Campbell, D. Sheberla, S. F. Liu, T. M. Swager, M. Dinca, *Angew. Chem., Int. Ed.* **2015**, *54*, 4349.

[17] a) W. Zhu, C. Zhang, Q. Li, L. Xiong, R. Chen, X. Wan, Z. Wang, W. Chen, Z. Deng, Y. Peng, *Appl. Catal., B* **2018**, *238*, 339; b) A. Nazir, H. T. T. Le, C.-W. Min, A. Kasbe, J. Kim, C.-S. Jin, C.-J. Park, *Nanoscale* **2020**, *12*, 1629; c) H. Wang, M. Miao, H. Li, Y. Cao, H. Yang, X. Ai, *ACS Appl. Mater. Interfaces* **2021**, *13*, 22505.

[18] Y. Li, S. Zheng, X. Liu, P. Li, L. Sun, R. Yang, S. Wang, Z. S. Wu, X. Bao, W. Q. Deng, *Angew. Chem., Int. Ed.* **2018**, *57*, 7992.

[19] Q. Gan, H. He, K. Zhao, Z. He, S. Liu, *J. Colloid Interface Sci.* **2018**, *530*, 127.

[20] M. Barczak, Y. Elsayed, J. Jagiello, T. J. Bandosz, *Electrochim. Acta* **2018**, *275*, 236.

[21] a) R. Kumar, S. Sahoo, E. Joanni, R. K. Singh, W. K. Tan, K. K. Kar, A. Matsuda, *Prog. Energy Combust. Sci.* **2019**, *75*, 100786; b) K. Wang, Y. Tang, Q. Jiang, Y. Lan, H. Huang, D. Liu, C. Zhong, *J. Energy Chem.* **2017**, *26*, 902.

[22] D. Chen, S. Huang, L. Zhong, S. Wang, M. Xiao, D. Han, Y. Meng, *Adv. Funct. Mater.* **2019**, *30*, 1907717.

[23] a) S. Haldar, K. Roy, R. Kushwaha, S. Ogale, R. Vaidhyanathan, *Adv. Energy Mater.* **2019**, *9*, 1902428; b) Z. Zhu, Y. Tang, Z. Lv, J. Wei, Y. Zhang, R. Wang, W. Zhang, H. Xia, M. Ge, X. Chen, *Angew. Chem., Int. Ed.* **2018**, *57*, 3656; c) Y. Lu, J. Nai, X. W. Lou, *Angew. Chem., Int. Ed.* **2018**, *57*, 2899.

[24] L. Cao, D. Li, T. Deng, Q. Li, C. Wang, *Angew. Chem., Int. Ed.* **2020**, *59*, 19292.

[25] Q. Wu, Y. Zheng, X. Guan, J. Xu, F. Cao, C. Li, *Adv. Funct. Mater.* **2021**, *31*, 2101034.

[26] X. Hu, X. Liu, K. Chen, G. Wang, H. Wang, *J. Mater. Chem. A* **2019**, *7*, 11016.

[27] Y. Zhong, F. Lin, M. Wang, Y. Zhang, Q. Ma, J. Lin, Z. Feng, H. Wang, *Adv. Funct. Mater.* **2020**, *30*, 1907579.

[28] X. Liu, W. Li, X. Zhao, Y. Liu, C.-W. Nan, L.-Z. Fan, *Adv. Funct. Mater.* **2019**, *29*, 1901510.

[29] C. Yang, Y. Yao, Y. Lian, Y. Chen, R. Shah, X. Zhao, M. Chen, Y. Peng, Z. Deng, *Small* **2019**, *15*, 1900015.

[30] L. Wang, Z. Wang, L. Xie, L. Zhu, X. Cao, *Electrochim. Acta* **2020**, *343*, 136138.

[31] Y. Liu, W. Li, Y. Xia, *Electrochem. Energy Rev.* **2021**, *4*, 447.

[32] G. Zheng, Z. Xing, X. Gao, C. Nie, Z. Xu, Z. Ju, *Appl. Surf. Sci.* **2021**, *559*, 149701.

[33] X. Cui, H. Dong, S. Chen, M. Wu, Y. Wang, *Batteries Supercaps* **2021**, *4*, 72.

[34] X. Zhao, H. Xu, Z. Hui, Y. Sun, C. Yu, J. Xue, R. Zhou, L. Wang, H. Dai, Y. Zhao, J. Yang, J. Zhou, Q. Chen, G. Sun, W. Huang, *Small* **2019**, *15*, 1904255.

[35] H. Xu, Y. Liu, T. Qiang, L. Qin, J. Chen, P. Zhang, Y. Zhang, W. Zhang, W. Tian, Z. Sun, *Energy Storage Mater.* **2019**, *17*, 126.